This manuscript was published in Journal of the American Ceramic Society, Volume 97, Issue 4, pages 1194-1201, April 2014. DOI: 10.1111/jace.12810

Plasticity controlled friction and wear in nanocrystalline SiC

Maneesh Mishra[1,2], Chaiyapat Tangpatjaroen[1,3], Izabela Szlufarska[1,3]

[1]Materials Science Program, University of Wisconsin Madison, Madison, WI-53706

[2]CMP Process R&D, Micron Technology, Inc., Boise, ID-83703

[3]Department of Materials Science and Engineering, University of Wisconsin-Madison, Madison, WI-53706

Abstract

Wear resistance of ceramics can be improved by suppressing fracture, which can be accomplished either by decreasing the grain size or by reducing the size of the deformation zone. We have combined these two strategies with the goal of understanding the atomistic mechanisms underlying the plasticity controlled friction and wear in nanocrystalline (nc) SiC. We have performed molecular dynamics simulations of nanoscale wear on nc-SiC with 5 nm grain diameter with a nanoscale cutting tool. We find that grain boundary (GB) sliding is the primary deformation mechanism during wear and that it is accommodated by heterogeneous nucleation of partial dislocations, formation of voids at the triple junctions, and grain pull-out. We estimate the stresses required for heterogeneous nucleation of partial dislocations at triple junctions and shear strength of GBs. Pile up in nc-SiC consists of grains that were pulled out during deformation. We compare the wear response of nc-SiC to single crystal (sc) SiC and show that scratch hardness of nc-SiC is lower than that of sc-SiC. Our results demonstrate that the higher scratch hardness in sc-SiC originates from nucleation and motion of dislocations whereas nc-SiC is more pliable due to additional mechanism of deformation via grain boundary sliding.

1. Background and motivation

Silicon carbide (SiC) exhibits good resistance to corrosive environments [1], is stable at high temperatures [2] and has excellent mechanical properties [3], e.g. high hardness. These properties make SiC a promising materials for such applications as high temperature coatings and microelectromechanical system (MEMS) [4,5]. Multiple experimental studies have been reported on nanoindentation and wear of SiC. For instance, Page *et. al*. [6] performed indentation testing with Berkovich pyramid-shape diamond indenter on single crystal (sc) SiC and showed that the dislocation nucleation takes place before any densification-induced phase transformation. Yan *et. al*. [7] studied the subsurface damage of sc-SiC in nanoindentation tests and reported formation of a polycrystalline structure with nanometer-sized grain in the indented region. Wear of SiC has been investigated for instance by Zum Gahr *et. al*. [8], who reported macro- and micro-tribological measurements of sc-SiC and nanocrystalline (nc) SiC. It was demonstrated that many factors such as the initial surface roughness, chemical composition at SiC surface, and humidity in air, can affect the coefficient of friction.

One of the major roadblocks in manufacturability and durability of SiC in the aforementioned engineering applications is that as a covalent ceramic SiC exhibits low fracture toughness, which compromises wear resistance of this material. Among the different ways to improve the wear resistance of ceramics, the following two are of particular interest to the current study: (a) decreasing the size of cutting tool, and (b) decreasing the grain size. Decreasing the size of the cutting tool decreases the size of the deformation zone, which lowers the probability of fracture by crack growth at existing flaws [9]. It has been reported that fracture toughness of ceramics can be increased by reducing the grain size to nanoscale [10,11,12]. The first approach has been successfully applied to machining of crystalline SiC. For example, Patten *et. al*. [13] showed that nanomachining of SiC with depths of cut smaller than 500 nm leads to ductile deformation and smooth surfaces after machining. Yin *et al*. [14] also reported ductile machining of SiC during grinding with diamond suspensions that had micrometerscale grit sizes. Decrease in the grain size has been shown to lead to dramatic changes in mechanical properties in both atomistic simulations and experiments [15,16,17]. Interestingly, it has been shown that in some cases both hardness and fracture toughness can be improved as SiC grain size is reduced to the nanoscale [16,18,19]. For instance, Vickers hardness of ~50 GPa and fracture toughness of ~4.8 $MPa.m^{1/2}$ have been reported for nc-SiC samples [16], which are high as compared to values of ~30 GPa and ~2.8 $MPa.m^{1/2}$ reported for single crystal SiC [16,18]. In this study, we focus on the deformation mechanisms during sliding wear in SiC, when both the grain size and the tool size are reduced to nanoscale. Deformation mechanisms in nc-SiC have been studied primarily during tensile deformation [17] and nanoindentation [15,16]. Wear response of SiC using nanoscale tools has been studied only for single crystal or polycrystalline samples [13,20] and it was shown that under these conditions wear of SiC is controlled by subsurface dislocation activity. It remains to be determined which deformation mechanisms, dislocation plasticity or (GB) deformation and sliding, control the tribological response of nc-SiC during frictional sliding and how the wear resistance of SiC is affected by simultaneous reduction in the tool size and the grain size. To provide answers to the aforementioned questions, we performed large scale molecular dynamics (MD) simulations of plasticity controlled single asperity sliding friction and wear on nc-SiC. This is the first study that elucidates the deformation mechanisms during sliding wear in this material. The details of the simulations are given in section 2. The atomistic mechanisms of sliding wear in nc-SiC are presented in section 3. In section 4, wear properties of nc-SiC are compared with those of single crystal SiC. For details of sliding wear of single crystal SiC, see Ref [20].

2. Simulation details

Large scale MD simulations of single asperity sliding wear have been performed on nc-SiC. The empirical potential used in this study was developed by Vashistha *et. al*. [21] and this potential has been shown to reproduce mechanical properties of SiC, such as hardness, fracture toughness and phase transformation pressure, in excellent agreement with experiments [21,22,23]. A cutting tool with a spherical tip of radius of curvature 10 nm is used. The tool tip is cut from an amorphous SiC (a-SiC) sample and the tip is then relaxed to minimize the surface energy. During the sliding simulations atoms in the tip are held fixed to isolate the effects of abrasion by a single asperity. Only the repulsive part of the interaction potential is used for tip-sample interactions. Adding adhesive interactions changes the contact area at a given normal load, but it does not affect the mechanisms of dislocation activity under the surface. Since here we are primarily interested in the plastic response of the material, excluding adhesive interactions between the tip and the sample is a reasonable approximation. The nc-SiC sample, consisting of 500 randomly oriented grains with an average grain diameter of 5.5 nm, was prepared by Voronoi construction [24,25]. The GB thickness in the simulated samples is in the range of 0.5-2 nm GB atoms are identified as those that have the centrosymmetry parameter [26] on their own sublattice different from that of the perfect fcc structure. Identification of GB atoms is not unique and the centrosymmetry analysis provides an approximate upper bound for GB thickness. Typical experimental values of GB thickness of SiC range from 0.5 nm to 3 nm. [27,28] Figure 1 shows the nc-SiC sample along with the grain size distribution. The system size is 355x355x355 $Å^3$. Sliding simulation has been performed at five different depths of cut in the range 0.5-5.5 nm. The depth of cut is calculated as the distance between the average height of the sample free surface and the lowest point on the spherical tip surface. The atoms in the bottom 2 nm region and 2 nm thick vertical region far away from the sliding tip are kept fixed throughout the simulations to provide rigid boundaries. All the simulations are carried out at 300 K using two Langevin thermostats. One of the thermostats is applied to the region around the sliding tip and moves at the same velocity as the sliding tip. The dimensions of the region, to which this thermostat is applied, are chosen to scale with the depth of cut. For example, the thermostat dimensions are 200x200x100 $Å^3$ and 200x200x160 $Å^3$ for depth of cut of 0.5 nm and 5.5 nm, respectively. The second Langevin thermostat is applied to the rest of the sample. Both thermostats are coupled to all components of velocities. Periodic boundary conditions are applied in the direction normal to the cutting direction. The tool tip is displaced by 0.015 Å every 20 time steps (where each time step Δt = 1.5 fs) giving an average sliding velocity of 50 m/s. The nc-SiC sample is equilibrated at 300 K before performing cutting simulations. The total friction force and the total normal load, respectively, are calculated in simulations by summing up forces on all the atoms of the tip along the lateral and the normal directions with respect to the sample surface. All quantities are averaged over at least 10 nm of sliding after the initial 5-10 nm of sliding to make sure the system has reached the steady state and the effects of initial cutting through a free standing edge are minimal. To understand the effect of GBs during sliding wear, the results of this study on nc-SiC are compared with sliding wear response observed in sc-SiC using the same nanoscale sliding tip. For sc-SiC, the details of simulation setup and mechanisms of material removal in sc-SiC have been reported in Ref. [20].

3. Atomistic mechanisms of wear in nc-SiC in single asperity contacts

Various studies of uniform deformation in nc-metals, both computational [25,29,30,31] and experimental [32,33,34,35], have shown that GB activity is the primary deformation mechanism at small grain sizes due to the increase in the volume fraction of the GB phase. Although relatively fewer studies have focused on nc-ceramics [15,17,36,37,38,39], it has been shown that enhanced GB activity leads to increased ductility of nc-ceramics as compared to their microcrystalline counterparts. At high

temperatures, diffusional transport can lead to GB migration and suppression of cavitation at GB junctions [40]. At low temperatures, GB sliding may occur either by motion of GB dislocations [40,41,42] or by local shear events [38,40,43,44]. In the presented study of single asperity sliding wear in nc-SiC, we find that deformation occurs by GB sliding, dislocation activity inside the grains and void formation at GB junctions. Dislocations nucleate heterogeneously at the sample surface and at the GB junctions. When the compatibility strains due to GB sliding cannot be relaxed by heterogeneous dislocation nucleation, void formation occurs at GB junctions. Each of the above deformation mechanisms is discussed in detail in the following subsections.

3.1 Grain boundary effects on material removal in nc-SiC

Mechanisms of material removal are different for sc and nc-SiC. Representative snapshots showing the material displaced to the front of the sliding tip at the depth of cut of 2.5 nm for both the sc-SiC and nc-SiC samples are shown in fig. 2. For sc-SiC, material displacement is assisted by glide and climb of dislocations nucleated at the tip sample interface [20]. When a dislocation reaches the surface of the sample ahead of the sliding tip, a surface step is formed. Successive formation of surface steps leads to formation of a pileup around the sliding tip as shown in fig 2(a). The details of the dislocation activity and wear mechanisms in sc-SiC have been provided in Ref [20]. For nc-SiC, material displacement occurs via grain pull-out to the surface as shown in fig. 2(b). As we will show later, the primary deformation mechanism in nc-SiC is GB sliding. In the case of near-surface GBs, sliding does not require any additional accommodation mechanisms and grains can be easily pushed out to the surface.

3.2 Accommodation mechanisms for GB sliding

As the sliding tip moves over the nc-SiC sample, the induced plastic strains are expected to lead to compatibility stresses at the GBs in the bulk of the material [40]. It has been shown that depending on the orientation of the grains linked at a GB, these stresses can lead to either emission of partial dislocations at the GB junctions [45] or void formation when dislocation nucleation from GB junctions is suppressed [46]. In addition, compatibility stresses may also be relaxed by GB migration which is not expected to be significant in ceramics at room temperature where thermally activated processes such as boundary or lattice diffusional transport and dislocation climb have high activation energies [40]. Here we first calculate shear stress required for GB sliding in nc-SiC during wear. Figure 3(b)-(c) shows an example of grain boundary slip observed in the MD simulations. In fig. 3(a), the resolved shear stress on the GB plane is shown as a function of tip displacement. For each atom in the GB, the calculated atomic stress tensor is resolved on the GB plane and along the sliding direction. The resolved shear stress on the GB is then calculated as an average over all the atoms in the GB. As shown in fig 3(a), as the resolved shear stress reaches ~5 GPa, slip occurs along the GB. We have calculated shear stresses for multiple GB interfaces where sliding was observed and found that stress required for sliding depends on the GB structure and position of the GB with respect to the sliding tip. The value calculated for resolved shear stress for different GBs in our study is in the range τ_{GB} = 5-11 GPa.

One should point out that a number of studies in literature have been dedicated [47,48,49,50,51] to developing phenomenological constitutive equations that relate the applied stress to the resulting strain rate in polycrystalline materials in the case when deformation is controlled by GB sliding. Models specific for nanocrystalline materials have also been reported [52]. These models have been summarized in Ref. [53] and the following mechanisms have been proposed to be responsible for deformation in nanocrystalline materials: (i) the primary deformation mechanism is GB sliding; (ii) GB sliding is accommodated by dislocation nucleation from GB junctions; (iii) dislocations pile up at a GB, exert a back stress and prevent other dislocations from propagating on the same slip system; (iv) climb

of the emitted dislocation is required to continue emission of dislocations from a GB junction and thereby to enable additional GB sliding. The deformation mechanisms found in our simulations are consistent with this overall picture, except that we do not observe dislocation climb in our study. In order to test quantitatively the specific phenomenological models, one needs to perform mechanical tests at a wide range of strain rates. Strain rates in MD simulations are currently limited to a relatively narrow range in the high strain rate regime (~10^8 s^{-1}). Consequently, these simulations do not provide an appropriate tool to test the aforementioned constitutive models. Nevertheless, a comparison can be made between MD simulations and mechanistic models that predict for example stresses required for nucleation of a dislocation from a GB junction, where the dislocation slip acts as an accommodation mechanism for GB sliding. Such comparison will be discussed in the next section.

3.2.1 Heterogeneous dislocation nucleation at GB

Figure 4(a) shows the resolved shear stress required for nucleation of a partial dislocation from a GB junction. The shear stress is calculated as an average over atoms at the GB junction and is resolved along the $[2\bar{1}1]$ direction on the $<11\bar{1}>$ plane in the grain containing the partial dislocation. The averages of resolved shear stress are calculated over the atoms in a spherical region (radius R) around the GB junction and are plotted in fig. 4(a). As the radius of the spherical region is decreased the shear stress required for nucleation of partial dislocation increases and converges to a value of τ_{pd} = 14 GPa for averaging radius *R* ~3Å. This value of nucleation stress for nucleation of leading partial from a GB junction in the simulations is in a good agreement with value of 13.1 GPa calculated using an analytical model [54]

$$\tau_{pd} = \sqrt{\frac{4G\gamma_{usf}}{\pi(1-\nu)d}} \qquad (1)$$

where, *d* is the grain diameter, γ_{usf} is the unstable stacking fault energy, *G* is the shear modulus and ν is the Poissons ratio. For SiC, γ_{usf} = 154 meV/Å^2, ν = 0.3 and *G* = 192 GPa [21]. The model given by eq. 1 is based on the assumption that the nucleation of a partial dislocation occurs when the unstable stacking fault energy γ_{usf} is equal to the energy released by the stress relaxation due to dislocation nucleation. To understand the deformation mechanisms in nc-SiC, the density of dislocations nucleated from the GB junctions is calculated as a function of the depth of cut and is plotted in fig. 5. The density of dislocations in both sc-SiC and nc-SiC samples is calculated as an average over at least 10 nm of sliding at each depth of cut. Also shown in fig. 5, are dislocation densities calculated for single asperity sliding wear on single crystal SiC along two mutually perpendicular directions (see Ref [20] for details). For nc-SiC, GB sliding is observed as the primary deformation mechanism. GB sliding compensates a significant fraction of strain applied by the sliding tip for depths of cut >1 nm. As a result, dislocation density observed in nc-SiC is lower than sc-SiC for depths of cut >1 nm. For the lowest depth of cut (0.5 nm), dislocation nucleation in the grains near the sliding interface is observed as the only deformation mechanism. Hence in the absence of GB sliding at the lowest depth of cut, dislocation density observed in nc-SiC is comparable to that in sc-SiC.

3.2.2 Void formation at GB junctions

When compatibility stresses at a GB junction cannot be relaxed by emission of partial dislocations, void formation occurs at the GB junctions. Formation of one such void at a GB junction observed during sliding wear in nc-SiC is shown in fig. 6. As the tip slides over the sample surface, slip occurs at the GB as shown by the dark gray (blue online) circles shown as reference atoms in fig. 6. In this case no dislocation nucleation at the GB junction is observed from the GB junction ahead of the sliding boundary.

4. Nanoscale wear resistance: sc-SiC v nc-SiC

In our study of deformation in nc-SiC, we observed both dislocation glide and GB sliding. In fig. 7, we have plotted normal load and friction force as a function of contact area at the five different depths of cut used in our simulations. Contact areas are calculated directly from MD simulations and they include the contribution from the elastic recovery in the wake of the moving tip. It is interesting to note that for both sc-SiC and nc-SiC, normal load is proportional to horizontal projection of contact area and friction force is proportional to vertical projection of contact area. As a result, both nc-SiC and sc-SiC show constant hardness and plastic zone under the sliding tip is fully developed. For sc-SiC, the value of hardness is found to be ~28 GPa, which is in agreement with values previously measured in experiments and simulations [16,55]. To investigate the wear performance of nc-SiC and compare it to sc-SiC, scratch hardness and specific wear rate were calculated for both sc-SiC and nc-SiC samples. Scratch hardness is a measure of the shear strength of the sliding interface [56], whereas specific wear rate represents the amount of material removed during sliding [57].

4.1 Scratch resistance

Scratch hardness is defined as the ratio of friction force and horizontal projection of tip-sample contact area [56]. At each depth of cut, scratch hardness is evaluated an average over at least 10 nm of sliding and the results are plotted in fig. 8(a). For depths of cut >1 nm, nc-SiC is found to have a lower scratch hardness than sc-SiC. In sc-SiC, deformation occurs via motion of dislocations. In sc-SiC, the hardness of material in front of the sliding tip originates from the stress required to nucleate and move the dislocations ahead of the sliding tip [20]. Nc-SiC deforms via dislocation motion inside the grains and sliding at the grain boundaries. As grain boundary sliding has a lower energy barrier, a significant fraction of applied strain is compensated by GB sliding and thus nc-SiC shows much lower dislocation density than sc-SiC (fig. 5). At the smallest depth of cut, deformation in nc-SiC occurs via heterogeneous dislocation nucleation from the tip/sample interface in the grains near the interface. As shown earlier in fig. 5, at the lowest depth of cut dislocation density in nc-SiC is comparable to that observed for sc-SiC. For example, for sliding along $<1\bar{1}0>$ in sc-SiC, a single dislocation half loop is nucleated under the sliding tip and glides ahead of the sliding tip. In sc-SiC, main contribution to hardness comes from the stress required to move the dislocation, i.e., Peierls stress. In nc-SiC, there GBs are an additional obstacle to deformation and act as barriers to glide of lattice dislocations. As a result, a comparable dislocation density in nc-SiC leads to a higher scratch hardness than sc-SiC at depth of cut of 0.5 nm.

To understand the role of dislocations in our sliding simulations in nc-SiC, scratch hardness is plotted as a function of dislocation density in fig. 8(b). It is interesting to note from fig. 8(b) that even though plasticity is well developed and normal hardness is independent of depth of cut and/or density of dislocations (fig. 7), scratch hardness is proportional to density of dislocations ahead of the sliding tip. This proportionality of scratch hardness with density of dislocations can be explained geometrically. Scratch hardness can be written as

$$SH = \frac{f_{friction}}{A_{hori}} = \left(\frac{f_{friction}}{f_{normal}}\right) \times \left(\frac{f_{normal}}{A_{hori}}\right) = \mu H_{nc} \quad (2)$$

where, μ is the coefficient of friction, A_{hori} is the horizontal projection of the tip-sample contact area, SH is the scratch hardness and H_{nc} is normal hardness during sliding in nc-SiC. We have shown in our earlier work [20] that m depends on depth of cut and dislocation density when plasticity is well developed, i.e., hardness is independent of dislocation density. Hence, the increase in scratch hardness with dislocation density during our sliding simulations has geometric origins. These results complement a recent study of deformation in ultrananocrystalline diamond, where, in absence of dislocation sources in ultrananocrystalline diamond, yield stress has no contribution from Peierls stress and is found tobe proportional to stress required for GB sliding [44].

4.2 Specific wear rate

Specific wear rate (W_{sp}) is defined as [57]

$$W_{sp} = \frac{V_T}{LF_n} \quad (3)$$

where V_T is the total amount of material removed over a sliding distance L at a normal load F_n. At each depth of cut, the total amount of material removed in simulations (V_T) is calculated as the product of atomic volume (Ω) and the number of atoms displaced by the sliding tip (N_{disp}). The atomic volume for both sc-SiC and nc-SiC is assumed to be Ω = 10.34 $Å^3$, which is the atomic volume for 3C-SiC zinc blende structure calculated by dividing the total volume of unit cell by the number of atoms in the unit cell. N_{disp} is calculated as the number of atoms above the sample surface as shown in fig. 9(a) for sc-SiC sample for depth of cut equal to 3.5 nm. Figure 9(b) shows the total volume of material displaced per unit normal load by the sliding tip as a function of the sliding distance for the sample shown in fig. 9(a). Specific wear rate W_{sp} in simulations is calculated as the slope of the plot in fig. 9(b). Figure 10(a) shows the specific wear rates for both sc-SiC and nc-SiC as a function of depth of cut. Nc-SiC has a higher wear rate than sc-SiC for all depths of cut used in simulations, which suggests that nc-SiC sample with grain size d = 5 nm is more pliable than sc-SiC sample when using a nanometer-sized tip. Higher wear rates for nc-SiC can also be explained by the fact that the nc-SiC sample under study exhibits a lower hardness (of ~20 GPa) than a single crystal sample as shown in fig 10(b). Higher wear rate for a material of lower hardness is consistent with Archards wear law [58]. The hardness of ~28 GPa for sc-SiC is in agreement with previously reported experimental values [16]. The softening of nc-SiC observed in our simulations is due to the pronounced GB sliding and suggests that the material is in the regime of the inverse Hall-Petch behavior [59,60,61,62]. It is intriguing that in our earlier MD simulations of nanoindentation of nc-SiC with grain size of approximately 8 nm we measured the hardness to be ~40 GPa [17], which is higher than the hardness of sc-SiC and which is consistent with the limited experimental data reported on nc-SiC [16]. Both, the previous and the current MD simulations employ the same empirical potentials and the same simulation protocols and therefore the observed difference in hardness is not an artifact of the simulation methodology. This difference in mechanical properties can be due either to the slightly smaller grain size in the current study as compared to the Ref. [16] or the different loading conditions. Specifically, in Ref. [16] the normal hardness was measured during normal loading (nanoindentation) and in the current study it is measured during lateral cutting, leading perhaps to different relaxation mechanisms in the two cases. The typical contact areas measured in the current simulations are also 2-3 times smaller than contact areas in Ref. [16]. It is possible that the effect of contact size is coupled to the

effect of the grain size, leading to a different balance of contributions from GB sliding and from dislocations to plasticity. A systematic investigation of the effects of grain size and the contact size on hardness and friction is beyond the scope of the current study.

Before concluding, it is instructive to ask what regime our simulations fall into with respect to the expected transition from ductile to brittle wear of SiC. The critical depth of cut (d_c) for such transition can be estimated from the following relation [63]

$$d_c = 0.15(E/H)(K_c/H)^2 \qquad (4)$$

where E is the Young modulus, H is the normal hardness, and K_c is the fracture toughness. For nc-SiC, we take H = 20 GPa, E = 200 GPa [17], and we approximate K_c to have the same value as in sc-SiC, which is 3 $MPa.m^{1/2}$. With these approximations, the calculated depth of cut is 14 nm, which is approximately three times the grain size. Since our maximum depth of cut in simulations is ~6 nm, the observed mechanisms of GB sliding and dislocation plasticity are consistent with being in the ductile regime of wear. This analysis further validates the idea that decreasing the size of the cutting tools to the nanometer regime is a promising avenue for suppressing the onset of brittle failure during wear of ceramics.

5. Conclusions

Using results from large scale MD simulations of single asperity sliding on nc-SiC (*d*=5 nm), wear performance of nc-SiC has been compared with that of sc-SiC. In particular, the atomistic mechanisms of material removal in nc-SiC have been investigated. Wear in nc-SiC shows a rich response with GB sliding as the primary deformation mechanism. Grain boundary sliding is accommodated by heterogeneous nucleation of partial dislocations, formation of voids at the triple junctions, and grain pull-out. The stress required for heterogeneous nucleation of partial dislocations at GB junctions and shear stress required for GB sliding have been calculated. Pile up in nc-SiC consists of grains that are pulled out during deformation. Similarly to sc-SiC, nc-SiC work hardens by subsurface dislocation activity, however unlike in sc-SiC plowing of nc-SiC in front of the sliding tip is accommodated by GB sliding. We have shown that on using nanoscale tools, nc-SiC exhibits a lower wear resistance and lower scratch hardness than that for sc-SiC. These results demonstrate that machining of nc-ceramics can be performed with nanometer-sized tools because in this regime brittle ceramics are pliable.

6 Acknowledgements

The authors are thankful for the financial support from NSF grant CMMI-0747661. The authors also acknowledge use of computational facilities supported by the University of Wisconsin Materials Research Science and Engineering Center (DMR-1121288) and use of the Center for Nanoscale Materials supported by the U. S. Department of Energy, Office of Science, Office of Basic Energy Sciences, under Contract No. DE-AC02-06CH11357.

References

1. R. G. Azevedo, J. Zhang, D. G. Jones, D. R. Myers, A. V. Jog, B. Jamshidi, M. B. J. Wijesundara, R. Maboudian, and A. P. Pisano, “Silicon Carbide Coated MEMS Strain Sensor for Harsh Environment Applications”; pp.643–646 in *IEEE 20th International Conference on Micro Electro Mechanical Systems (MEMS)*. Hyogo, Japan, 2007.

2. G. Gradinaru, T. S. Sudarshan, S. A. Gradinaru, W. Mitchell, and H. M. Hobgood, “Electrical Properties of High Resistivity 6H–SiC under High Temperature/High Field Stress,” *Appl. Phys. Lett*., **70** [6] 735-737 (1997).
3. X. Li and B. Bhushan, “Micro/Nanomechanical Characterization of Ceramic Films for Microdevices,” *Thin Solid Films*, **340** [1-2] 210–217 (1999).
4. M. Mehregany, C. A. Zorman, S. Roy, A. J. Fleischman, C. H.Wu, and N. Rajan, “Silicon Carbide for Microelectromechanical Systems,” *Int. Mater. Rev*., **45** [3] 85–108 (2000).
5. C. A. Zorman and R. J. Parro, “Micro- and Nanomechanical Structures for Silicon Carbide MEMS and NEMS,” *Phys. Status Solidi B*, **245** [7] 1404–1424 (2008).
6. T. F. Page, W. C. Oliver, and C. J. McHargue, “The Deformation Behavior of Ceramic Crystals Subjected to Very Low Load (Nano)indentations,” *J. Mater. Res.*, **7** [2] 450–473 (1992).
7. J. Yan, X. Gai, and H. Harada, ”Subsurface Damage of Single Crystalline Silicon Carbide in Nanoindentation Tests,” *J. Nanosci. Nanotechno*., **10** [11] 7808–7811 (2010).
8. K. H. Zum Gahr, R. Blattner, D. H. Hwang and K. P¨ohlmann, “Micro- and Macro-Tribological Properties of SiC Ceramics in Sliding Contact,” *Wear*, **250** [1-12] 299–311 (2001).
9. J. J. Cao, W. J. MoberlyChan, L. C. De Jonghe, C. J. Gilbert, and R. O. Ritchie, “In Situ Toughened Silicon Carbide With Al-B-C Additions,” *J. Am. Ceram. Soc.*, **79** [2] 461–469 (1996).
10. S. V. Bobylev, A. K. Mukherjee, I. A. Ovid’ko, and A. G. Sheinerman, “Amorphous Intergranular Boundaries as Toughening Elements in Nanocrystalline,” *Rev. Adv. Mater. Sci*., **21** [1] 99–105 (2009).
11. X. Wang, N. P. Padture, H. Tanaka, and A. L. Ortiz, “Wear-Resistant Ultra-Fine-Grained Ceramics,” *Acta Mater.*, **53** [2] 271–277 (2005).
12. N. P. Padture, “In Situ-Toughened Silicon Carbide,” *J. Am. Ceram. Soc.*, **77** [2] 519–523 (1994).
13. J. Patten, W. Gao, and K. Yasuto, “Ductile Regime Nanomachining of Single-Crystal Silicon Carbide,” *J. Manuf. Sci. Eng.*, **127** [3] 522–532 (2005).
14. L. Yin, E. Y.J. Vancoille, K. Ramesh, and H. Huang, “Surface Characterization of 6H-SiC (0001) Substrates in Indentation,” and Abrasive Machining. *Int. J. Mach. Tool Manu*., **44** [6] 607–615 (2004).
15. I. Szlufarska, A. Nakano, and P. Vashishta, “A Crossover in the Mechanical Response of Nanocrystalline Ceramics,” *Science*, **309** [5736] 911–914 (2005).
16. F. Liao, S. L. Girshick, W. M. Mook, W. W. Gerberich, and M. R Zachariah, “Superhard Nanocrystalline Silicon Carbide Films,” *Appl. Phys. Lett.*, **86** [17] 171913 (2005).
17. Y. Mo and I. Szlufarska, “Simultaneous Enhancement of Toughness, Ductility, and Strength of Nanocrystalline Ceramics at High Strain-Rates,” *Appl. Phys. Lett.*, **90** [18] 181926 (2007).
18. M. J. Slavin and G. D. Quinn, “Mechanical Property Evaluation at Elevated Temperature of Sintered b-Silicon Carbide,” *Int. J. High Technol. Ceram.*, **2** [1] 47 – 63 (1986).
19. Y. Zhao, J. Qian, L. L. Daemen, C. Pantea, J. Zhang, G. A. Voronin, and T.W. Zerda, “Enhancement of Fracture Toughness in Nanostructured Diamond–SiC Composites,” *Appl. Phys. Lett.*, **84** [8] 1356–1358 (2004).
20. M. Mishra and I. Szlufarska, “Dislocation Controlled Wear in Single Crystal Silicon Carbide,” *J. Mater. Sci.*, **48** [4] 1593–1603 (2012).
21. P. Vashishta, R. K. Kalia, A. Nakano, and J. P. Rino, “Interaction Potential for Silicon Carbide: A Molecular Dynamics Study of Elastic Constants and Vibrational Density of States for Crystalline and Amorphous Silicon Carbide,” *J. Appl. Phys.*, **101** [10] 103515 (2007).
22. H. Kikuchi, R. K. Kalia, A. Nakano, P. Vashishta, P. S. Branicio, and F. Shimojo, “Brittle Dynamic Fracture of Crystalline Cubic Slicon Carbide (3C-SiC) via Molecular Dynamics Simulation,” *J. Appl. Phys.*, **98** [10] 103524 (2005).
23. F. Shimojo, I. Ebbsjö, R. K. Kalia, A. Nakano, J. P. Rino, and P. Vashishta, “Molecular Dynamics Simulation of Structural Transformation in Silicon Carbide under Pressure,” *Phys. Rev. Lett.*, **84** [15] 3338–3341 (2000).

24. G. Voronoi, ”Nouvelles Applications des Paramètres Continus à La Théorie des Formes Quadratiques,” *J. Reine Angew. Math.*, **1908** [134] 199–287 (1908).
25. J. Schiøtz, F. D. Di Tolla and K. W. Jacobsen, “Softening of Nanocrystalline Metals at Very Small Grain Sizes,” *Nature*, **391** [6667] 561–563 (1998).
26. A. Stukowski, “Structure Identication Methods for Atomistic Simulations of Crystalline Materials,” *Modelling Simul. Mater. Sci. Eng*., **20** [4] 045021 (2012).
27. X. F. Zhang, G. Y. Lee, D. Chen, R. O. Ritchie, and L. C. De Jonghe, ”AbrasiveWear Behavior of Heat-Treated ABC Silicon Carbide,” *J. Am. Ceram. Soc.*, **86** [8] 1370 – 1378 (2003).
28. S. Tsurekawa, S. Nitta, H. Nakashima, and H. Yoshinaga, “Grain Boundary Structures in Silicon Carbide: Verification of the Extended Boundary Concept,” *Interface Sci.*, **3** [1] 75 – 84 (1995).
29. H. Van Swygenhoven and P. A. Derlet, “Grain-Boundary Sliding in Nanocrystalline FCC Metals,” *Phys. Rev. B*, **64** [22] 224105 (2001).
30. V. Yamakov, D. Wolf, S. R. Phillpot, A. K. Mukherjee, and H. Gleiter, “Deformation-Mechanism Map for Nanocrystalline Metals by Molecular-Dynamics Simulation,” *Nature Mater.*, **3** [1] 43-47 (2004).
31. A. Hasnaou, H. Van Swygenhoven, and P. M. Derlet, “Cooperative Processes During Plastic Deformation in Nanocrystalline FCC Metals a Molecular Dynamics Simulation,” *Phys Rev B*, **66** [18] 184112 (2002).
32. K. S. Kumar, H. Van Swygenhoven, and S. Suresh, “Mechanical Behavior of Nanocrystalline Metals and Alloys,” *Acta Mater.*, **51** [19] 5743–5774 (2003).
33. A. V. Sergueeva, N. A. Mara, N. A. Krasilnikov, R. Z. Valiev, and A. K. Mukherjee, “Cooperative Grain Boundary Sliding in Nanocrystalline Materials,” *Philos. Mag.*, **86** [36] 5797–5804 (2006).
34. Y. Ivanisenko, L. Kurmanaeva, J.Weissmueller, K. Yang, J. Markmann, and H. Rosner, “Deformation Mechanisms in Nanocrystalline Palladium at Large Strains,” *Acta Mater.*, **57** [11] 3391–3401 (2009).
35. N. Q. Chinh, P. Szommer, Z. Horita, and T. G. Langdon, “Experimental Evidence for Grain Boundary Sliding in Ultrafine-Grained Aluminum Processed by Severe Plastic Deformation,” *Adv. Mater.*, **18** [1] 34–39 (2006).
36. A. Gallardo-López, A. Domnguez-Rodrguez, C. Estourns, R. Marder, and R. Chaim, “Plastic Deformation of Dense Nanocrystalline Yttrium Oxide at Elevated Temperatures,” *J. Eur. Ceram. Soc.*, **32** [12] 3115–3121 (2012).
37. A. Dominguez-Rodriguez, D. Gomez-Garcia, E. Zapata-Solvas, J. Z. Shen, and R. Chaim, “Making Ceramics Ductile at Low Homologous Temperatures,” *Scripta Mater.*, **56** [2] 89–91 (2007).
38. H. Conrad, J. Narayan, and K. Jung, “Grain Size Softening in Nanocrystalline Tin,” *Int. J. Refrct. Met. H.*, **23** [4-6] 301–305 (2005).
39. M. J. Roddy, W. R. Cannon, G. Skandan, and H. Hahn, “Creep Behavior of Nanocrystalline Monoclinic ZrO_2,” *J. Eur. Ceram. Soc.*, **22** [14-15] 2657–2662 (2002).
40. A. P. Sutton and R. W. Balluffi, Interfaces in Crystalline Materials. Clarendon Press, Oxford, 1995.
41. M. Yu. Gutkin, I. A. Ovid’ko, and N. V Skiba, “Crossover from Grain Boundary Sliding to Rotational Deformation in Nanocrystalline Materials,” *Acta Mater.*, **51** [14] 4059–4071 (2003).
42. M. Yu. Gutkin, I. A. Ovid’ko, and N. V Skiba, “Strengthening and Softening Mechanisms in Nanocrystalline Materials under Superplastic Deformation,” *Acta Mater.*, **52** [6] 1711–1720 (2004).
43. S. V. Bobylev, M.Yu. Gutkin, and I. A. Ovid’ko, “Partial and Split Dislocation Configurations in Nanocrystalline Metals,” *Phys. Rev. B*, **73** [6] 064102 (2006).
44. Y. Mo, D. Stone, and I. Szlufarska, “Strength of Ultrananocrystalline Diamond Controlled by Friction of Buried Interfaces,” *J. Phys. D: Appl. Phys.*, **44** [40] 405401 (2011).
45. A. G. Froseth, P. M. Derlet, and H. Van Swygenhoven, “Dislocations Emitted from Nanocrystalline Grain Boundaries: Nucleation and Splitting Distance,” *Acta Mater.*, **52** [20] 5863–5870 (2004).
46. M. J. Demkowicz, A. S. Argonz, D. Farkas, and M. Frary, “Simulation of Plasticity in Nanocrystalline Silicon,” *Philos. Mag.*, **87** [28] 4253–4271 (2007).

47. M. F. Ashby, and R. A. Verrall, “Diffusion-Accommodated Flow and Superplasticity,” *Acta Metall. Mater.*, **21** [2] 149–163 (1973).
48. A. Ball, and M. M. Hutchison, “Superplasticity in the AluminiumZinc Eutectoid,” *Met. Sci.*, **3** [1] 1–7 (1969).
49. A. K. Mukherjee, “The Rate Controlling Mechanism in Superplasticity,” *Mater. Sci. Eng.*, **8** [2] 83–89 (1971).
50. R. C. Gifkins, “Grain-Boundary Sliding and Its Accommodation During Creep and Superplasticity,” *Metall. Trans. A*, **7** [7-8] 1225–1232 (1976).
51. T. G. Langon, “A Unified Approach to Grain Boundary Sliding in Creep and Superplasticity,” *Acta Metall. Mater.*, **42** [7] 2437–2443 (1994).
52. H. H. Fu, D. J. Benson, and M. A. Meyers, “Analytical and Computational Description of Effect of Grain Size on Yield Stress of Metals,” *Acta Mater.*, **49** [13] 256 –2582 (2001).
53. H. Watanabe, T. Mukai, and K. Higashi, “Deformation Mechanism of Fine-Grained Superplasticity in Metallic Materials Expected from the Phenomenological Constitutive Equation,” *Mater. Trans.*, **45** [8] 2497–2502 (2004).
54. R. J. Asaro and S. Suresh, “Mechanistic Models for the Activation Volume and Rate Sensitivity in Metals with Nanocrystalline Grains and Nano-Scale Twins,” *Acta Mater.*, **53** [12] 3369–3382 (2005).
55. H. P. Chen, R. K. Kalia, A. Nakano, P. Vashishta, and I. Szlufarska, “Multimillion-Atom Nanoindentation Simulation of Crystalline Silicon Carbide: Orientation Dependence and Anisotropic Pileup,” *J. Appl. Phys.*, **102** [6] 063514 (2007).
56. J. A. Williams, “Analytical Models of Scratch Hardness,” *Tribol. Int.*, **29** [8] 675–694 (1996).
57. D. A. Rigney, “Sliding Wear of Metals,” *Annu. Rev. Mater. Sci.*, **18** 141–163 (1988).
58. J. F. Archard, ”Contact and Rubbing of Flat Surfaces,” *J. Appl. Phys.*, **24** [8] 981–988 (1953).
59. C. C. Koch and J. Narayan, ”The Inverse Hall-Petch Effect - Factor Artifact?”; pp. 634 in *MRS Symposium Proceedings*. 2001.
60. C. A. Schuh, T. G. Nieh, and T. Yamasaki, “Hall-Petch Breakdown Manifested in Abrasive Wear Resistance of Nanocrystalline Nickel,” *Scripta Mater.*, **46** [10] 735–740 (2002).
61. D. Wolf, V. Yamakov, S. R. Phillpot, A. Mukherjee, and H. Gleiter, “Deformation of Nanocrystalline Materials by Molecular-Dynamics Simulation Relationship to Experiments?,” *Acta Mater.*, **53** [1] 1–40 (2005).
62. K. A. Padmanabhan, G. P. Dinda, H. Hahn, and H. Gleiter, “Inverse Hall-Petch Effect and Grain Boundary Sliding Controlled Flow in Nanocrystalline Materials,” *Mater. Sci. Eng. A*, **452-453** 462–468 (2007).
63. T. G. Bifano, T. A. Dow, and R. O. Scattergood, “Ductile-Regime Grinding: A New Technology for Machining Brittle Materials,” *J. Eng. Ind.*, **113** [2] 184–189 (1991).

Figure captions

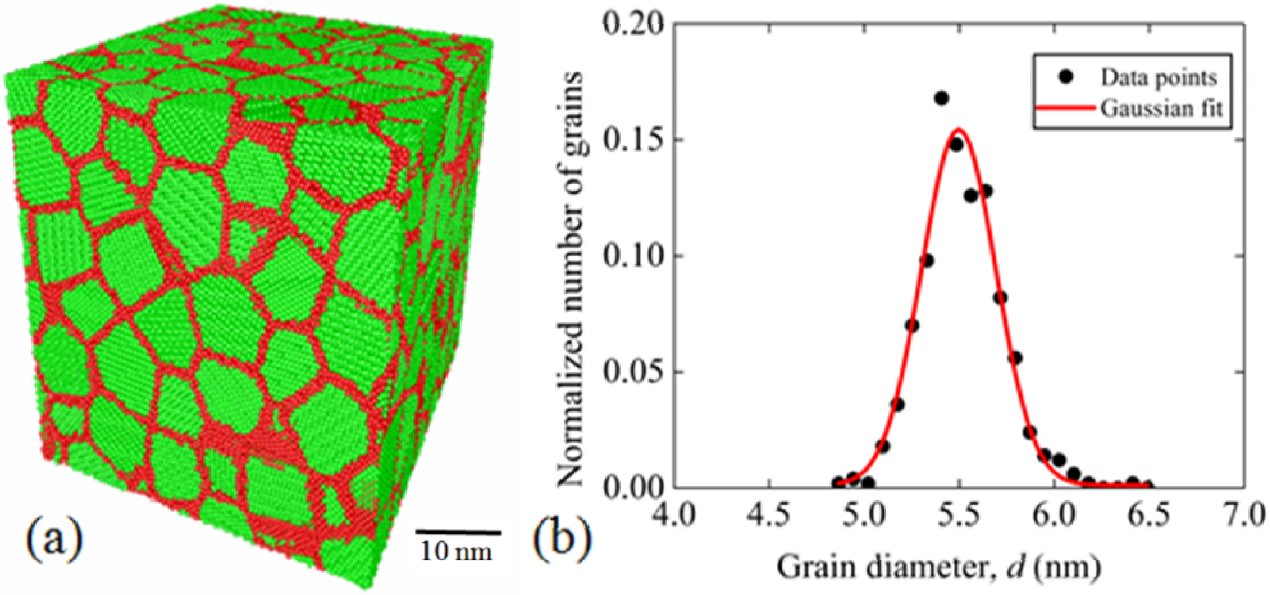

Fig. 1: (a) Nanocrystalline SiC sample showing the 3-D GB structure prepared by the Voronoi construction [24,25]. The sample consists of 500 grains and the volume fraction of the GB phase is 0.256. (b) Grain size distribution for the nc-SiC sample.

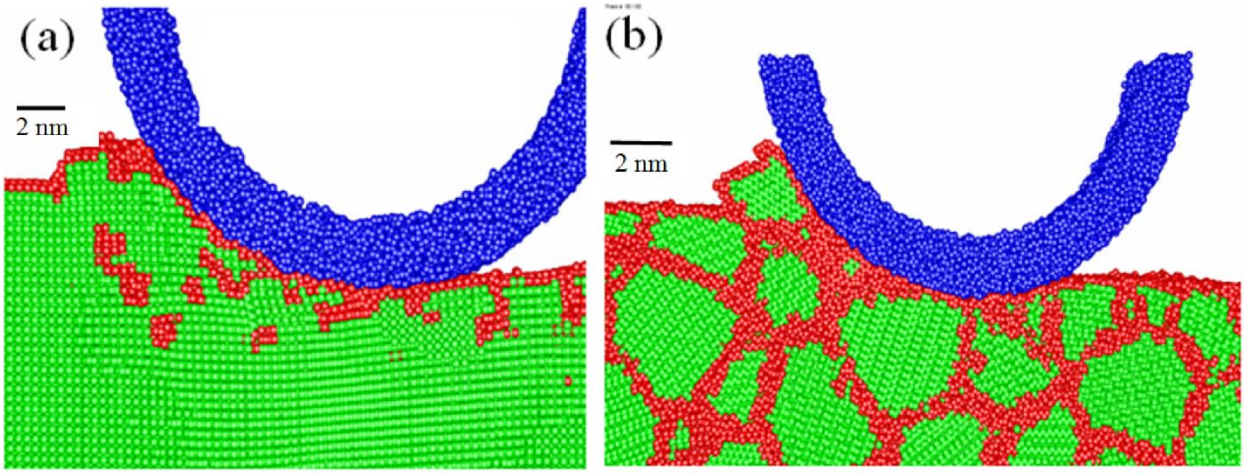

Fig. 2: Atomistic snapshots of material displacement in (a) sc-SiC and (b) nc-SiC with grain size 5 nm using a R=10 nm sliding tip. Material displacement (grain pull-out) to the surface of nc-SiC sample occurs via grain boundary sliding. Dark gray (blue online) circles represent atoms in the tip. Light gray (green online) and medium gray (red online) spheres represent, respectively, atoms with and without perfect zinc blende order.

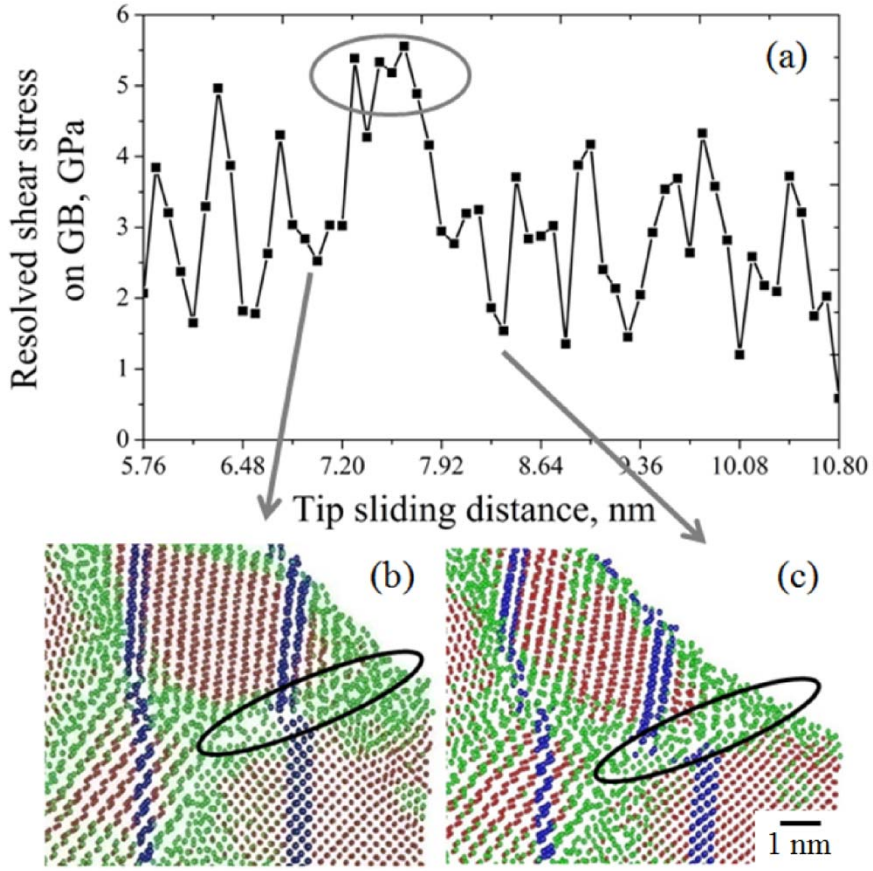

Fig. 3: (a) Resolved shear stress on the GB is shown as a function of tip sliding distance. (b)-(c) The atomic snapshots show the deformation in nc-SiC due to GB sliding. Light gray (green online) and medium gray (red online) circles, respectively, represent atoms in the GB and the neighboring grains. Dark gray (blue online) circles represent atoms in a vertical column to shown the orientation of grains before and after slip at the GB.

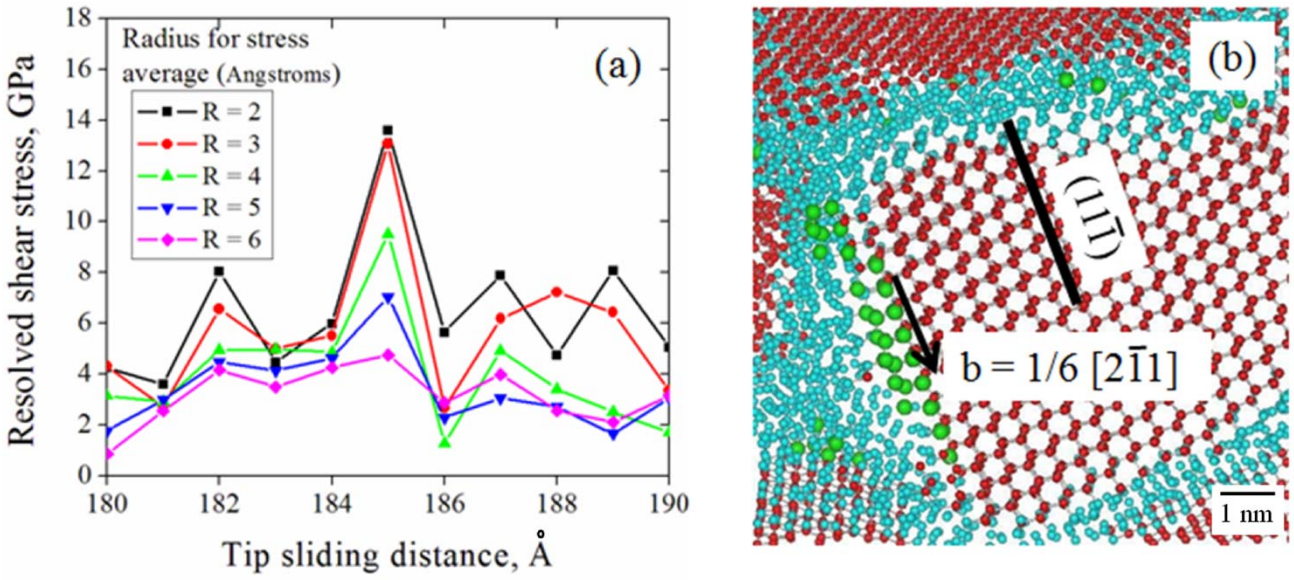

Fig. 4: (a) Resolved shear stress at a GB junction during dislocation nucleation as calculated for various radii R for stress averaging. (b) A snapshot of dislocation nucleation showing the direction of Burgers vector. Dark gray (red online) and light gray (blue online) circles, respectively, represent atoms with perfect zinc blende structure and atoms in the GB. Medium gray (green online) circles represent atoms in the leading partial dislocation nucleated at the triple junction.

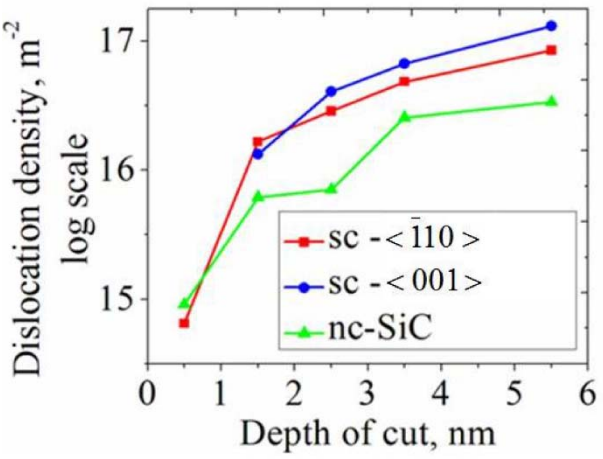

Fig. 5: Dislocation density ahead of the sliding tip plotted as a function of depth of cut. For depths of cut larger than 1 nm, nc-SiC has a lower dislocation density than sc-SiC.

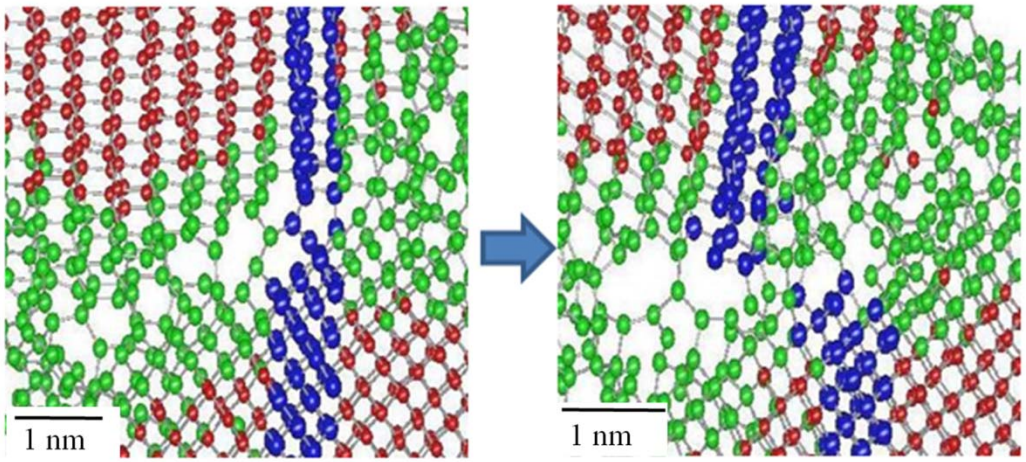

Fig. 6: Void formation at GB junction due to GB sliding. Light gray (green online) and medium gray (red online) circles, respectively, correspond to atoms in the GB and neighboring grains. Dark gray (blue online) circles represent atoms in a vertical column before and after occurance of sliding at the GB. The snapshot shows a 20 Å thick vertical cross section of the sample under the sliding tip.

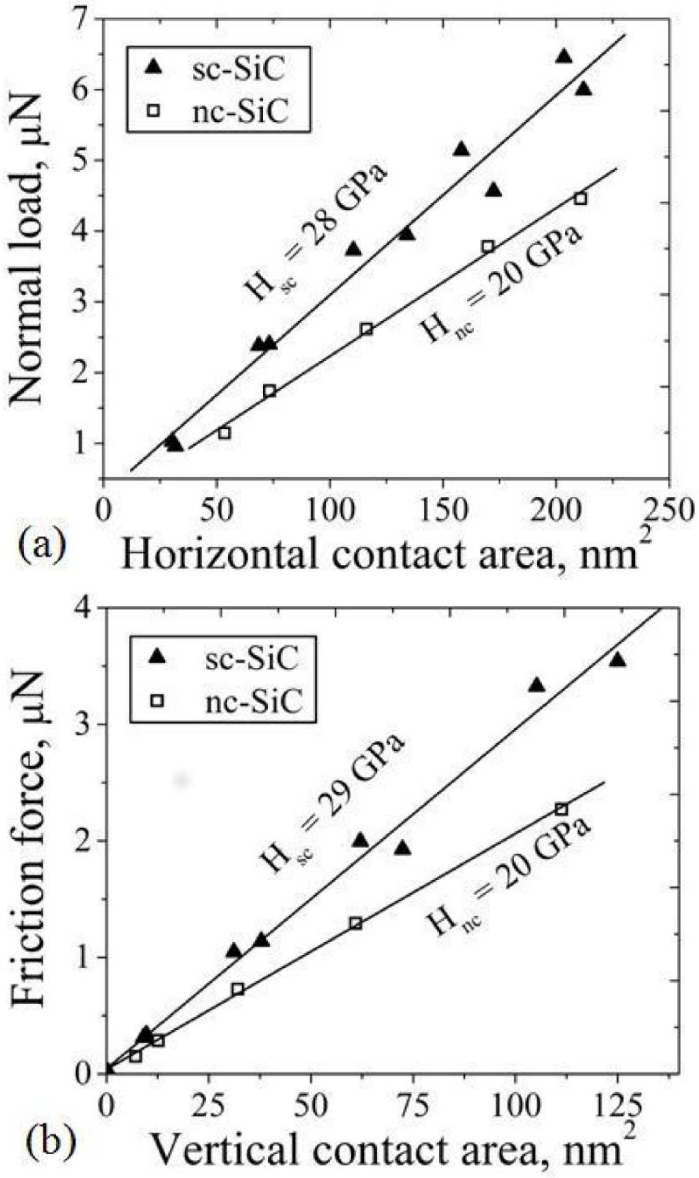

Fig. 7: (a) Normal load and (b) Friction force plotted as a function of horizontal projection of contact area of the sliding interface for sc-SiC and nc-SiC samples. H_{sc} and H_{nc}, respectively, represent hardness of the single crystal and nc-SiC sample. The horizontal and vertical contact areas are calculated during contact under load. Elastic recovery does occur in the wake of the moving tip and this contribution is accounted for in the calculation of contact area.

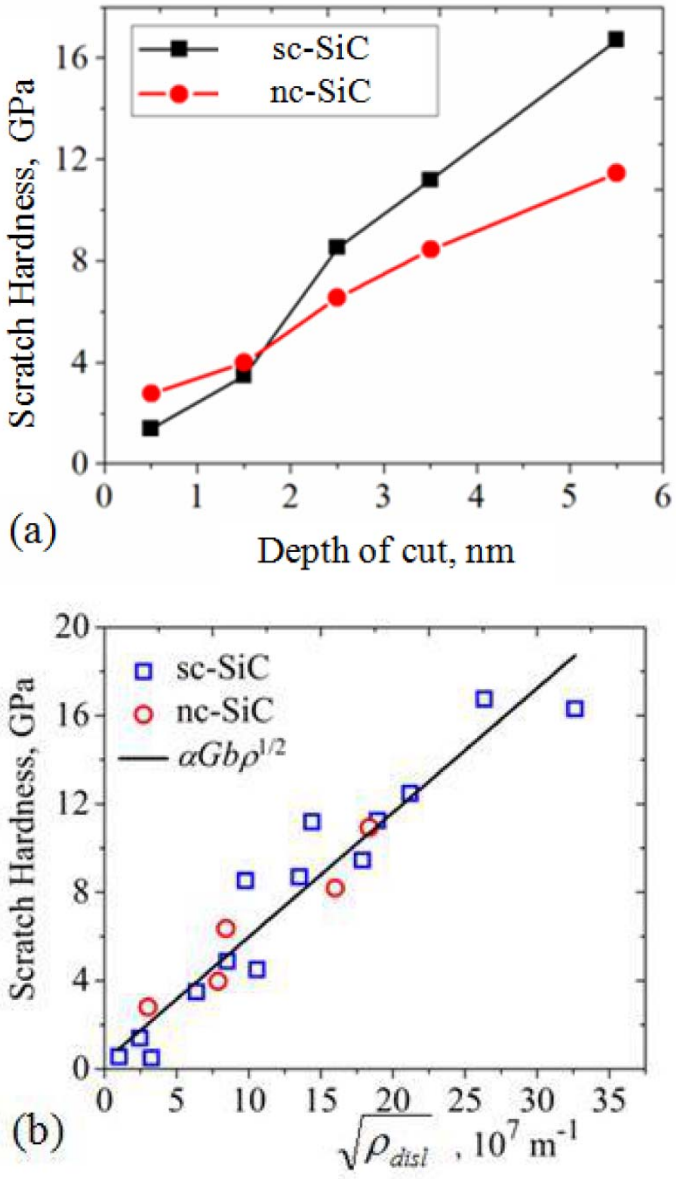

Fig. 8: (a) Scratch hardness of single crystal and nanocrystallineSiC samples shown as a function of depth of cut. (b) Scratch hardness of sc-SiC and nc-SiC plotted as a function of dislocation density ahead of the sliding tip.

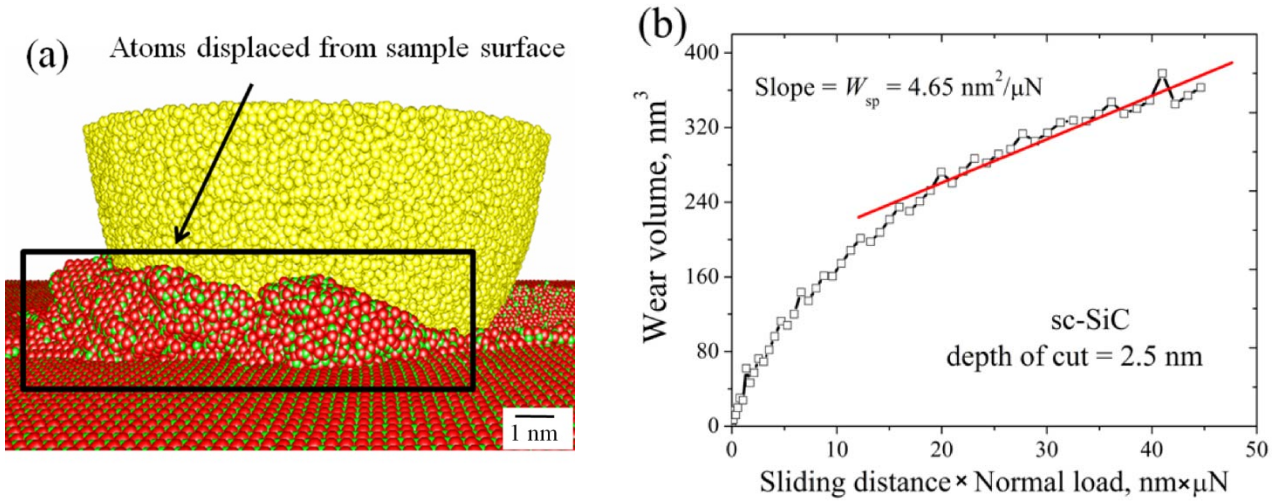

Fig. 9: (a) Snapshot from MD simulations showing atoms displaced on the sc-SiC sample surface at depth of cut of 3.5 nm. The number of atoms shown in the rectangular box is used to calculate the total wear volume as explained in text. (b) Specific wear rate is calculated as the slope of the wear volume vs. work done by the sliding tip (product of sliding distance and normal load) during sliding.

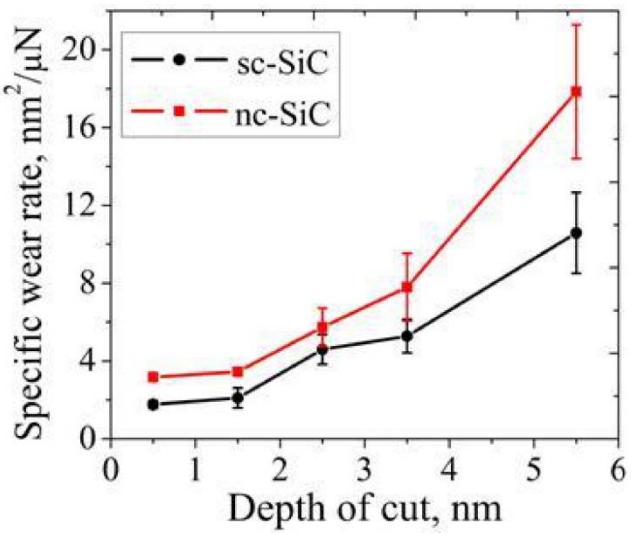

Fig. 10: Specific wear rate for single asperity sliding on sc-SiC and nc-SiC as a function of depth of cut.